Materials Today Physics 25 (2022) 100715

Contents lists available at ScienceDirect

Materials Today Physics

journal homepage: www.journals.elsevier.com/materials-today-physics

Coral-like hierarchically nanostructured membrane with high free volume for salt-free solar-enabled water purification

Jincui Gu [a,b], Peng Xiao [a,b,*], Jianmin Guan [a], Feng Ni [a], Chang Zhang [a], Weiqing Yang [a], Qingquan Liu [c], Tao Chen [a,b,**]

[a] Key Laboratory of Marine Materials and Related Technologies, Zhejiang Key Laboratory of Marine Materials and Protective Technologies, Ningbo Institute of Material Technology and Engineering, Chinese Academy of Science, Ningbo, 315201, China
[b] School of Chemical Sciences, University of Chinese Academy of Science, Beijing, 100049, China
[c] School of Materials Science and Technology, Hunan Provincial Key Laboratory of Advanced Materials for New Energy Storage and Conversion, Hunan University of Science and Technology, Xiangtan, 411201, China

ARTICLE INFO

Keywords:
Hierarchical nanostructure
Free volume
Salt-resistant
Anti-fouling
Solar evaporation

ABSTRACT

Solar evaporation presents a sustainable means to alleviate global water shortages. Varying photothermal materials have been designed to enhance evaporation performance. However, the critical technology gap is their low efficiency due to the severe salt crystallization and organic pollution. Here, we proposed a coral-like polypyrrole (PPy)-based photothermal membrane by the interface modification of d-glucitol (DG) and tetrakis (hydroxymethyl)phosphonium chloride (THPC). The designed PPy@DG/THPC membrane exhibited a wide range of sunlight absorption capacity with an efficiency of ~97.6% due to its hierarchical nanostructure. Moreover, this membrane displayed superhydrophilicity and rich charges, giving it a superior salt-resistance property. Furthermore, molecular dynamics simulations indicated that this membrane exhibited a high free volume to inhibit salt crystallization. Hence, the evaporation rate of the PPy@DG/THPC membrane reached 1.46 ± 0.02 kg/m^2/h in simulated brine (3.5 wt% NaCl) under 1-sun illumination. Besides, it exhibited exceptional anti-fouling ability under the synergy of hydration and charge effects. Overall, this membrane can achieve effective and sustainable solar evaporation to produce freshwater water to meet drinking-water standards. This work will offer a new approach to developing efficient solar evaporation for water remediation.

1. Introduction

Water shortage is an urgent global challenge that threatens the continuity of humankind and society [1–3]. Some strategies are explored to address this issue. Recently, solar evaporation has attained extensive interest because solar power is a renewable and clean energy source [4–8]. Solar-to-thermal conversion materials are critical to harvesting light in solar evaporation systems [9–15]. Tremendous efforts are committed to developing photothermal materials. For example, plasmonic nanoparticles, carbon-based materials, polymeric membranes, carbonized biomass materials, sponges, and hydrogel, were constructed [16–27]. They can improve their solar evaporation process through several approaches, such as water evaporation enthalpy regulation, heat energy loss management, light-to-heat conversion enhancement [28]. However, due to the rapid localized heat and interfacial steam generation, salts may accumulate and block the passage of steam evaporation, inevitably resulting in a sharp reduction of light-to-heat conversion capacity [11,29–33].

Numerous attempts have been undertaken to solve this problem. On the one hand, some strategies, such as washing crystalline salt and salt ion diffusion backflow, have been proposed [34–36]. Hu et al. reported a 3D plasmonic wood to generate solar steam. It showed a high light absorption capacity (~99%). A spontaneous thermal salt transportation gradient formed at night due to the differentiated pore structure in the wood inner [34]. Therefore, the accumulated salts can gradually dissolve into the microchannels after the evaporation progress. On the

* Corresponding author. Key Laboratory of Marine Materials and Related Technologies, Zhejiang Key Laboratory of Marine Materials and Protective Technologies, Ningbo Institute of Material Technology and Engineering, Chinese Academy of Science, Ningbo, 315201, China.
** Corresponding author. Key Laboratory of Marine Materials and Related Technologies, Zhejiang Key Laboratory of Marine Materials and Protective Technologies, Ningbo Institute of Material Technology and Engineering, Chinese Academy of Science, Ningbo, 315201, China.
E-mail addresses: xiaopeng@nimte.ac.cn (P. Xiao), tao.chen@nimte.ac.cn (T. Chen).

https://doi.org/10.1016/j.mtphys.2022.100715
Received 22 March 2022; Received in revised form 28 April 2022; Accepted 9 May 2022
Available online 11 May 2022

other hand, some Janus structures are constructed to weaken salt crystallization [37,38]. Xu et al. reported a Janus photothermal material with penetrative cone-like pores for solar-driven water purification [11]. It showed an excellent light absorption property (>97%), and the water output was up to 1.1 kg m^{-2} h^{-1}. Zhu et al. reported a Janus absorber through electrospinning for solar desalination [39]. The hydrophobic layer was used for light absorption, and the hydrophilic layer was applied to pump water. Its evaporation rate was ~1.3 kg m^{-2} h^{-1} under 1-sun. Despite this progress, the evaporation performance should be further enhanced [40–42]. In addition, the interface fouling arising from organic pollutants is a critical challenge. These contaminants may evaporate with water, bringing about secondary pollution, and might even be enriched in the water system [21]. Therefore, it is highly desired to design advanced photothermal materials that possess exceptional salt-rejection ability to guarantee solar evaporation and bear excellent anti-fouling to effectively inhibit the evaporation of organic contaminants [23,29].

An ideal photothermal material should have the following characteristics. For one thing, its particular structure endows itself with good light-to-heat conversion ability [43,44]. For another, it should have abundant charges to enhance salt-resistance ability [4,30]. Besides, the interaction between water and contaminants should allow water evaporation but block the others [44,45]. Herein, a coral-like polypyrrole (PPy)-based hierarchically nanostructured membrane was prepared by the interfacial functionalization of d-glucitol (DG) and tetrakis (hydroxymethyl)phosphonium chloride (THPC) (Fig. 1A–C). PPy was modified with the d-glucitol through the supramolecular hydrogen bond (H-bond) to improve the structural stability and enhance the hydrophilicity of the PPy membrane (Fig. 1D).

Moreover, the THPC molecule showed a good affinity for water molecules because of its large hydrophilic functional groups [46,47]. THPC was further functionalized to endow the PPy@DG membrane with

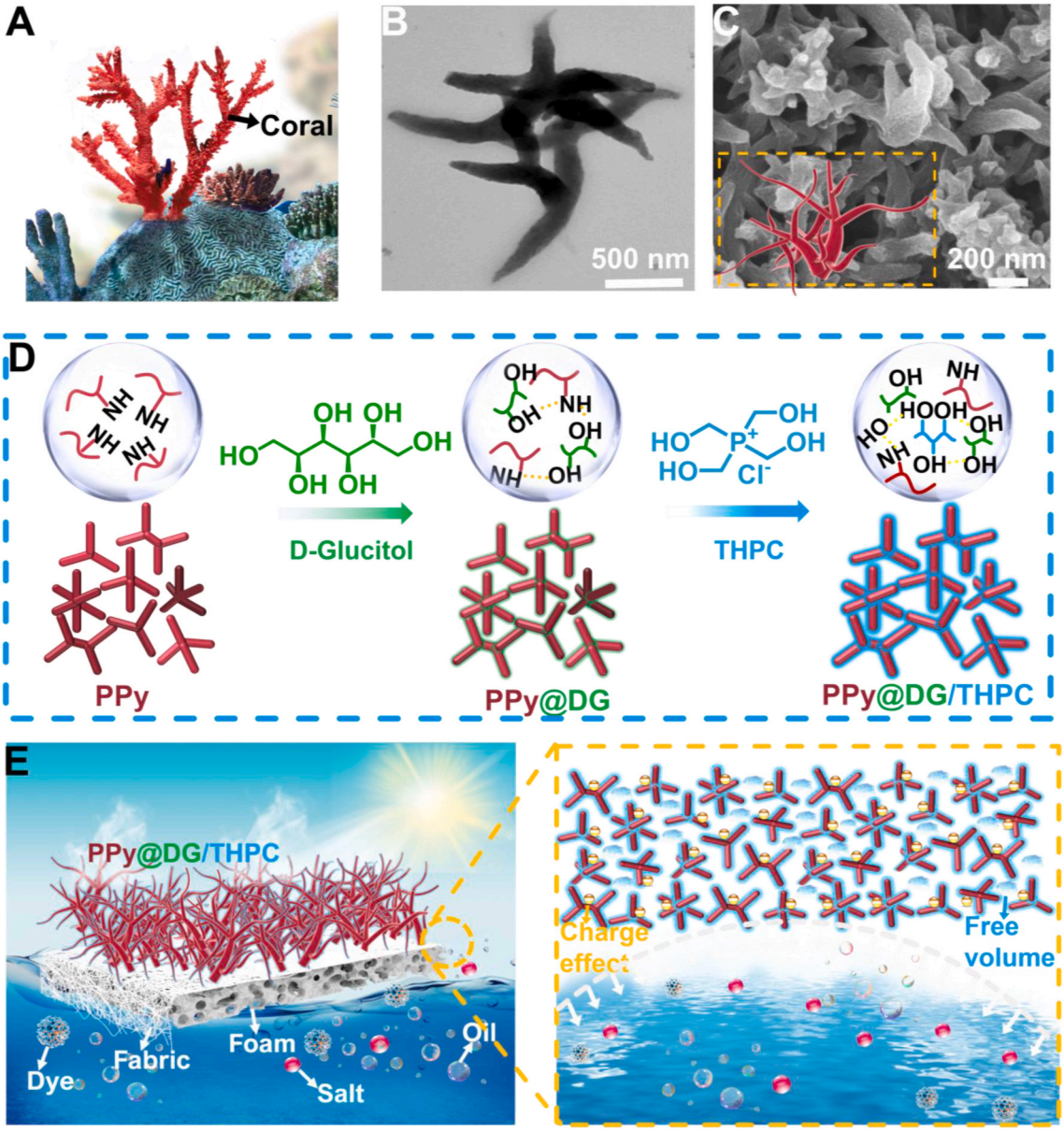

Fig. 1. Schematic illustration of the preparation of the coral-like hierarchically PPy@DG/THPC nanostructured membrane for solar-driven water harvest. (A) Photo of the coral in the water. (B) TEM image of the coral-like PPy@DG/THPC. (C) SEM image of the coral-like PPy@DG/THPC and its schematic structure. (D) The coral-like PPy was modified with DG and THPC through the supramolecular H-bond. (E) Schematic diagram of the PPy@DG/THPC membrane for efficient solar evaporation. This membrane was endowed with a coral-like structure for broad sunlight absorption and fast water molecule transmission. Moreover, it possessed abundant charges and enhanced free volume for improved salt-resistance and anti-fouling abilities.

rich charges (Fig. 1D). The obtained PPy@DG/THPC membrane exhibited superb light-absorbing ability with an efficiency of ~97.6% due to its hierarchical nanostructure. Molecular dynamics simulations indicated this membrane presented a higher free volume because of the THPC molecule's tetrahedral structure, facilitating the inhibition of salt crystallization [48–50]. Therefore, this membrane exhibited a satisfactory salt-resistant capacity with an evaporation rate of up to 1.46 ± 0.02 kg/m^2/h after 20 cycles of evaporation process under 1-sun illumination (Fig. 1E). Furthermore, it presented an excellent anti-fouling ability due to the THPC introduction. This work offers a new clue to construct advanced photothermal materials for salt-free solar-enabled water purification.

2. Experiment

2.1. Materials

Pyrrole, dopamine, d-glucitol (DG), tetrakis (hydroxymethyl)phosphonium chloride (THPC), 4-dimethylaminopyridine (DMAP) were purchased from Sigma-Aldrich Co, Ltd. 1-Aminopyridinium iodide (1-APi) and 1-Ethylpyridinium bromide ([EtPy][Br]), were purchased from Aladdin (Shanghai) Co, Ltd. Ferric chloride ($FeCl_3$), sodium chloride (NaCl), and copper chloride ($CuCl_2$) were bought from Sigma-Aldrich Co, Ltd. Chloroform, heptane and dichloroethane were got from Aladdin (Shanghai) Co, Ltd. Dye molecules, including methyl orange (MO), methylene azure II (MAII), methyl blue (MB), evans blue (EB), rose bengal-94 (RB-94) were bought from Sigma-Aldrich Co, Ltd. Other solvents were purchased from Sigma-Aldrich Co, Ltd. The substance was purchased from Millipore Industrial & Lab Chemicals.

2.2. Preparation of the PPy nanorods

The PPy nanorods were prepared according to the previous report [46]. Specifically, 520 μL of pyrrole and 0.2 g of dopamine were dissolved in 20 mL of water and then stirred for 30 min in an ice bath. 4.8 g of $FeCl_3$ was dissolved in 25 mL of water and ultrasound at 100 Hz for 15 min to obtain a uniform $FeCl_3$ solution. Then the $FeCl_3$ solution was added to the pyrrole dopamine system and kept stirring for 9 h in an ice bath at 300 rpm. Subsequently, the mixture was rinsed with water and ethanol 6 times to remove the unreacted pyrrole monomer. Lastly, the PPy nanorod was obtained by drying at 60 °C for 8 h. The role of PDA can be explained from the following aspects. On the one hand, there were abundant amino and phenolic hydroxyl groups on the PDA molecule, providing a platform for material engineering functionalization. On the other hand, as previously reported, the morphology of PPy is influenced by the preparation process [46]. Introducing PDA will facilitate the formation of PPy nanorods.

2.3. Preparation of PPy@DG membrane

PPy was dispersed in water and ultrasound at 300 Hz for 1 h to get a homogeneous dispersion (2 mg/mL). The d-glucitol was added into water and stirred for 30 min under 25 °C to obtain a homogeneous solution (2 mg/mL). Then, the PPy dispersion with varying volumes (1–4 mL) was filtrated onto the substance under 0.03 Mpa and dried under 60 °C for 4 h. Subsequently, the PPy membrane was soaked into the d-glucitol solution (2 mg/mL, 4 mL) at room temperature for 30 min. The PPy@DG membrane was rinsed with water and ethanol alternately 6 times to remove the residue. Lastly, the PPy@DG membrane was obtained by drying at 60 °C for 4 h.

2.4. Preparation of the coral-like PPy@DG/THPC membrane

Different concentrations of THPC dispersions were prepared by adjusting the relative dosage of THPC, DMAP, and water. The mass ratio between THPC and DMAP was fixed at 4:1. The concentration of THPC solutions was 5%–35%, respectively. Then, the PPy@DG membrane was immersed into the THPC solutions for 1 h under 45 °C, respectively. Subsequently, the PPy@DG/THPC membrane was repeatedly rinsed with water and alcohol to remove the residual THPC. Lastly, it was dried in the vacuum oven under 40 °C for 2 h to obtain the PPy@DG/THPC membrane.

2.5. Preparation of the PPy@DG//1-APi and PPy@DG/[EtPy][Br] membranes, respectively

As comparative experiments, the PPy@DG//1-APi and PPy@DG/[EtPy][Br] membranes were prepared, respectively. Firstly, 0.50 g of 1-APi and [EtPy][Br] were dispersed into 2.83 mL of water and ultrasound for 10 min to get the 1-APi and [EtPy][Br] solutions with the concentration of 15%, respectively. Secondly, the PPy@DG membranes were immersed into the 1-APi and [EtPy][Br] solutions for 30 min at 25 °C to get the 1-APi and [EtPy][Br] modified PPy@DG composite membranes, respectively. Thirdly, these membranes were placed into the vacuum oven under 40 °C for 2 h. Lastly, these membranes were rinsed with water and ethanol alternately three times and dried at 60 °C to obtain the PPy@DG/1-APi composite membrane and PPy@DG/[EtPy][Br] membrane, respectively.

2.6. Solar-driven water purification

The photothermal membrane (2.5 × 2.5 cm^2) was placed on a non-woven fabric. This system was transferred on a foam. Then, the above configuration was set on a beaker filled with 80 mL of water. The non-woven fabric was used to absorb and transport water to the surface of the photothermal membranes. The foam acted as a support layer and thermal isolation. A thermal insulator was used to wrap the beaker to eliminate the light entry effects. Afterwards, a beaker containing various solutions was illuminated under a specific solar simulator to assess the water evaporation. The mass change was recorded using an electronic scale. Noting: each experiment was carried out under the intensity of 1000 W/m^2 (1-sun illumination) there were special requirements. To ensure the accuracy of the data, we set the ambient temperature of photothermal evaporation as 26 °C, and the ambient humidity as 40%. Besides, each membrane was wet during the solar evaporation in this work.

2.7. Calculation of evaporation efficiency

The evaporation efficiency (η) of the PPy@DG/THPC-15 photothermal membrane for saline water (3.5 wt%) was calculated using the following equation:

$$\eta = m\Delta H/AQ$$

In this formula, m represented the mass flux during irradiation. △H was the equivalent total evaporation enthalpy of the water molecule. A stood for the surface area of this membrane. Q was the power density of solar irradiation.

2.8. Characterization

The micromorphology was obtained from the scanning electronic microscopy (SEM, Hitachi S4800, Japan) and transmission electronic microscopy (TEM, JEOL2100 HR, America). The cross-sectional micromorphology was performed on the scanning electronic microscopy, (SEM, Hitachi S4800, Japan). The roughness was observed through atomic force microscopy (AFM, Bruker Dimension ICON, America). A confocal laser scanning microscope (CLSM, Zeiss LSM 700, Germany) was applied to record the morphological images. The wettability was received from the contact angle measuring instrument (OCA-20, Data physics, America) at room temperature. Different locations were studied to acquire the average value. Zeta potential analyzer (Zeta, Nano ZS,

England) was used to test the zeta potentials. The chemical compositions were received from the energy-dispersive X-ray spectroscopy (EDS, Thermo Scientific, USA). Fourier-transform infrared spectroscopy (FTIR, Bruker TENSOR II) was exploited to test the chemical constituents. The thermal degradation process was assessed from the thermogravimetric analysis (TG, Perkin Elmer STA600, America). X-ray photoelectron spectroscopy (XPS, Thermo Fisher ESCALAB 250Xi, Japan) was applied to analyze the element content of each membrane. Dynamic light scattering (DLS) was used to record the size distribution of the feed and filtration. The light absorption ability was investigated through the ultraviolet–visible (UV/Vis) spectrometer spectrophotometer (Perkin Elmer, Lambda 950, America). The temperature change was monitored by the IR thermal camera (Optris PI 400, Germany). The conductivity was carried out on the conductivity tester (AZ8361, China). The ion concentrations were analyzed using the inductively coupled plasma atomic emission spectroscopy (ICP-AES, NexION 300, America). The concentration of dyes and emulsions was analyzed through the UV–Visible spectrometer (UV–Vis, Lambda 950, Japan).

3. Results and discussion

The photothermal membrane was obtained through interface modification. Scanning electron microscopy (SEM) and transmission electronic microscopy (TEM) were carried out to characterize the microstructure of polypyrrole (PPy) before and after modification. As shown in Fig. 2A-**2B**, the PPy took on a rod-like structure, which assembled randomly to form the coral-like PPy membrane. However, due to the weak interaction of the pyrrole molecules, large pores even cracks appeared inside the PPy membrane (Fig. 2C, S1A) [10,51]. However, after modifying the d-glucitol (DG) molecules, the irregular aperture structure gradually decreased, and the PPy@DG membrane became dense (Fig. 2D, Figures S1-S2). This result suggested that the d-glucitol molecules were taken on a role of a bridge to make PPy@DG membrane and substance combined tightly.

Furthermore, after the introduction of tetrakis (hydroxymethyl) phosphonium chloride (THPC) molecules, the PPy@DG/THPC membrane was more uniform than the PPy@DG membrane (Fig. 2E). The pore size of the PPy@DG/THPC membrane was 250–350 nm, which was smaller than the PPy@DG membrane (Fig. 2F). These results indicated the THPC molecule was successfully functionalized on the PPy@DG membrane. The average diameter of the PPy nanorods was also studied. As shown in Fig. 2G-**2I**, the average diameter of the PPy@DG/THPC (90–125 nm) was higher than the PPy@DG (80–105 nm) and PPy (70–90 nm), further proving the modification of DG and THPC molecules. The cross-section SEM images of the PPy@DG and PPy@DG/THPC membranes were also investigated. As shown in Fig. 3A, the thickness of the PPy@DG membrane was 16.2 ± 1.4 μm. There was a litter change after modifying the THPC molecules (17.6 ± 0.6 μm) (Fig. 3B). Moreover, the micromorphology of the PPy@DG/THPC membrane indicated its dense porous compacted network structure (Fig. 3C). The interlaced architecture will endow the PPy@DG/THPC membrane with fast water molecules' transmission capacity [41,42].

The chemical composition of the PPy@DG/THPC membrane was studied through the Fourier-transform infrared spectroscopy (FTIR). The sharp absorption peak at ~1029.8 cm^{-1} and ~1664.9 cm^{-1} were attributed to the C–P stretching vibrations in the PPy@DG/THPC membrane (Fig. 3D) [47]. There was a weak absorption peak at ~1186.2 $cm^{-1}$and ~1398.1 cm^{-1}, proving the presence of (C–P) in the THPC structure (Fig. 3D) [52–54]. Thermogravimetric (TG) analysis was also used to assess the mass change of different membranes. As displayed

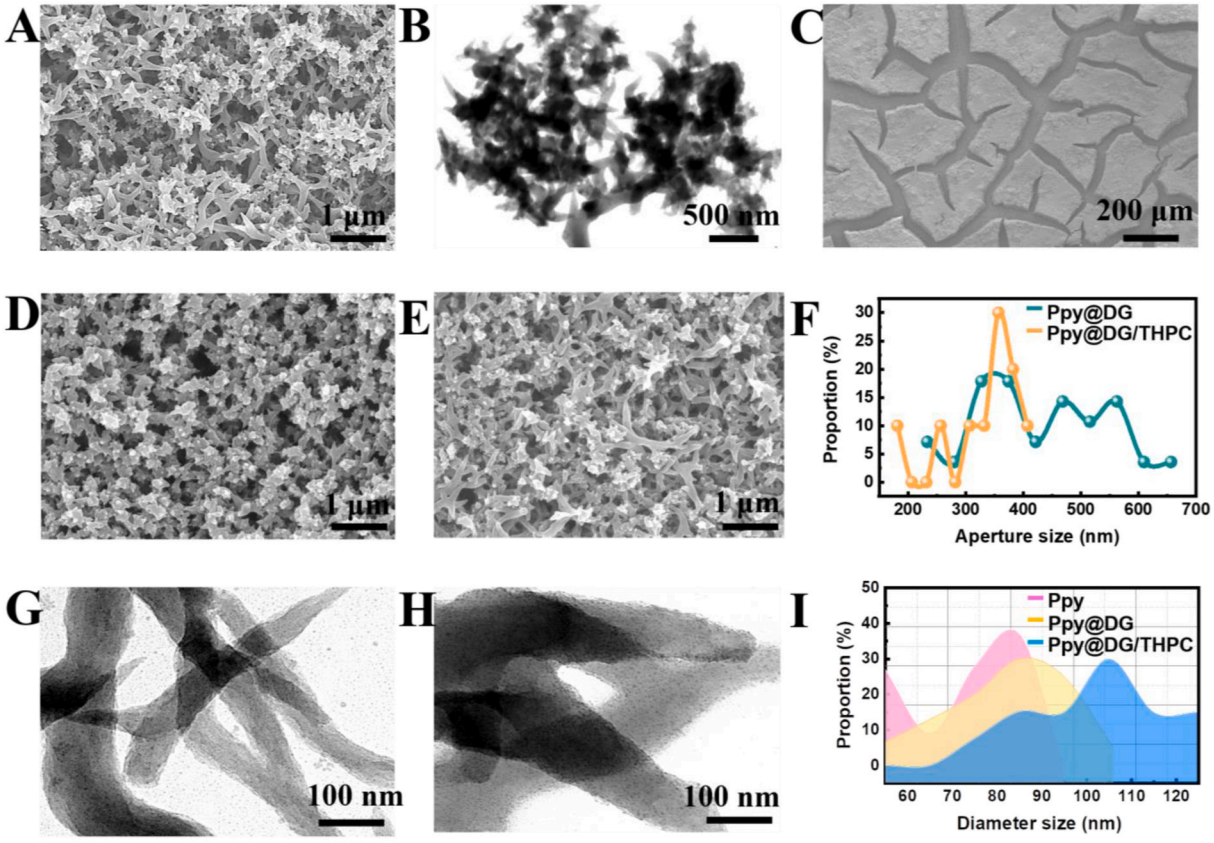

Fig. 2. (A) SEM image of the PPy membrane. (B) TEM image of the PPy nanorods. SEM images of the (C) PPy membrane, (D) PPy@DG membrane, and (E) PPy@DG/THPC membrane, respectively. (F) Pore sizes of the PPy@DG membrane and PPy@DG/THPC membrane. TEM images of the (G) PPy@DG and (H) PPy@DG/THPC. (I) Diameter size distributions of the PPy membrane, PPy@DG membrane, and PPy@DG/THPC membrane.

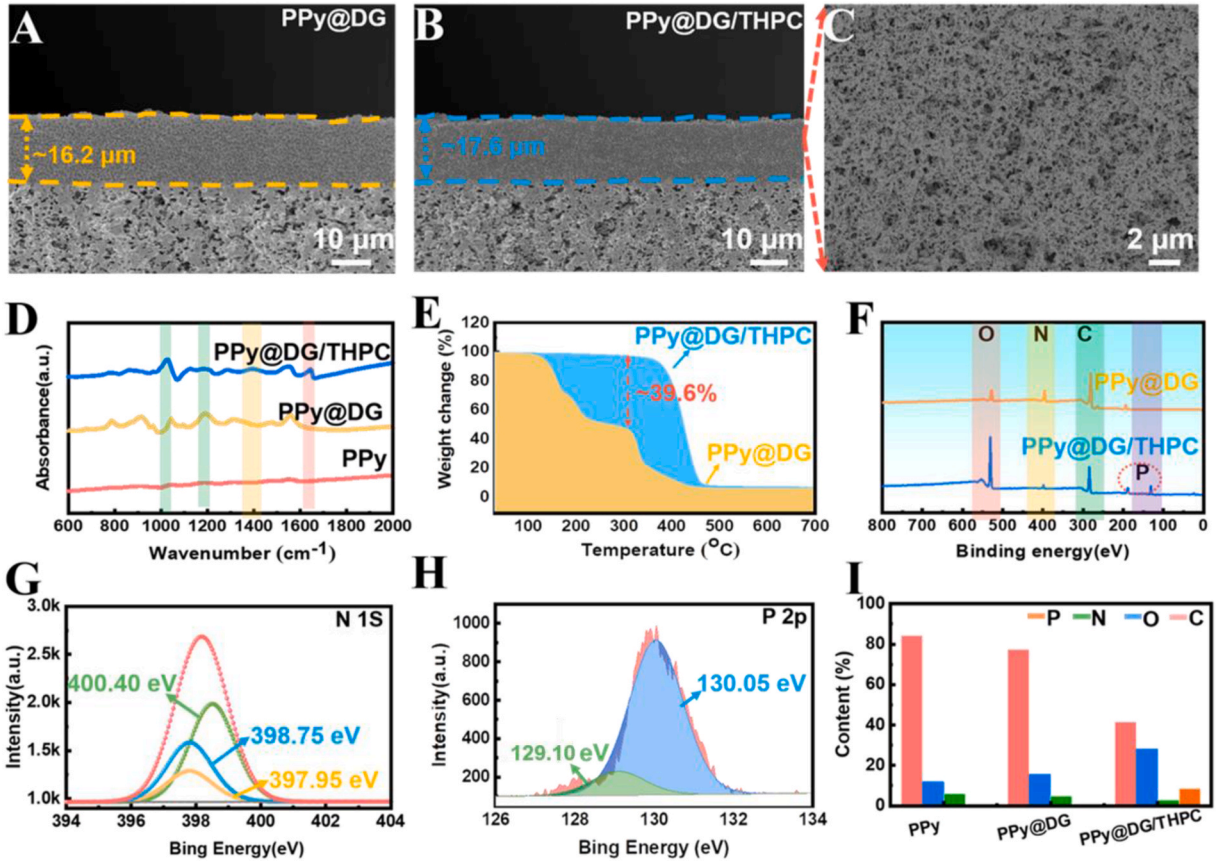

Fig. 3. Cross-sectional SEM images of (A) the PPy@DG membrane and (B) the PPy@DG/THPC membrane. (C) SEM image of the cross-section topography of the PPy@DG/THPC membrane. (D) FTIR spectra of the PPy membrane, PPy@DG membrane, and PPy@DG/THPC membrane. (E) TGA results of the PPy@DG membrane and PPy@DG/THPC membrane. (F) XPS spectrum of the PPy@DG membrane and PPy@DG/THPC membrane. (G) N1s spectrum of the PPy@DG/THPC membrane. (H) P 2p spectrum of the PPy@DG/THPC membrane. (I) Element contents in the PPy membrane, PPy@DG membrane, and PPy@DG/THPC membrane.

in Fig. 3E, there were ~39.6% mass changes, intimating the loss of the hydrogen and oxygen atoms from the THPC. In addition, X-ray photoelectron spectroscopy (XPS) was performed to test the chemical composition of the PPy@DG and PPy@DG/THPC membrane. As shown in Fig. 3F, both O 1s (~540 eV), N 1s (~398 eV), and C 1s (~284 eV) existed in these membranes, which was consistent with the TEM and SEM energy spectrums (Figure S3-S4). Figure S5 showed the three peaks of C1s at ~283.4 eV, ~284.1 eV, and ~285.2 eV, corresponding to the-C═O, C–C, and C═C, respectively [45,54]. In addition, the peaks at ~400.40 eV, ~398.75 eV, ~397.95 eV were assigned to the C–NH_2, C_3N, C–N═C groups from the dopamine, respectively (Fig. 3G), [54].

Furthermore, the P element existed in the PPy@DG/THPC membrane but was not observed in the PPy@DG membrane. Also, there were two peaks at ~130.05 eV and ~129.10 eV in the P 2p, inferring –OCH_2-*P*–H_2CO– and- OCH_2–*P*-, respectively (Fig. 3H) [53,54]. Besides, there was a noticeable element change between the PPy@DG membrane and PPy@DG/THPC membrane (Fig. 3I). The N element content in the PPy@DG membrane was slightly higher than that in the PPy@DG/THPC membrane (Fig. 3I). In comparison, the P element presented an opposite trend (Fig. 3I). These results also proved the functionalization of the THPC in the PPy@DG/THPC membrane. XPS was also used to study the element changes of the PPy@DG/THPC membrane with different THPC contents. As shown in Fig. 4A, the contents of the C element showed a gradual decrease with THPC content increase, which showed an opposite trend with the P element. Moreover, a slight change occurred in the element content when the dosage of the THPC was up to 15%. SEM image was further used to characterize the structural changes of the PPy@DG/THPC with different THPC contents. As shown in Fig. 4B-**4C**, the average diameter of the PPy@DG/THPC-25 and PPy@DG/THPC-35 was ~128 nm and ~136 nm, respectively. These results indicated that excessive content of THPC (>15%) has a litter effect on the morphology of the Py@DG/THPC membrane.

The confocal laser scanning microscope (CLSM) was employed to characterize the fine microstructure of these membranes. The roughness of the PPy@DG/THPC-15 membrane (0.520 ± 0.02 μm) was lower than the PPy membrane (0.726 ± 0.07 μm) and PPy@DG membrane (0.708 ± 0.04 μm) (Fig. 4D-**4F**). This change was consistent with the atomic force microscopy (AFM) images. The roughness of the PPy@DG/THPC-15 membrane was 165.2 ± 17.9 nm, which was smoother than the PPy@DG membrane (316.3 ± 29.8 nm) (Fig. 4G-**4H**, **S6**). The reduced roughness can promote the low resistance transmission of water molecules [44,54,55]. Furthermore, the PPy@DG/THPC membrane's roughness with different THPC contents was studied. As presented in Fig. 4I and Figure S7, the surface roughness decreased along with the increasing amount of THPC, and there was litter change when the THPC's content was above 15%.

The wetting behavior of the PPy-based membrane was further investigated using the water contact angle (WCA) measurement. The PPy membrane showed superhydrophilicity that it took ~4.0 s for water to penetrate its internal network (Fig. 5A). However, the PPy@DG membrane was more hydrophilic with a spread time of ~3.0 s. This result was attributed to the abundant hydroxyl functional groups in the DG molecules. The penetration process of the Py@DG/THPC-15 membrane was faster than the PPy membrane and PPy@DG membrane, indicating the THPC functionalization on the PPy@DG membrane. The wettability of the PPy@DG/THPC membrane with different contents of THPC was studied. The water molecule penetration times of the PPy@DG/THPC-10 membrane and PPy@DG/THPC-20 membrane were

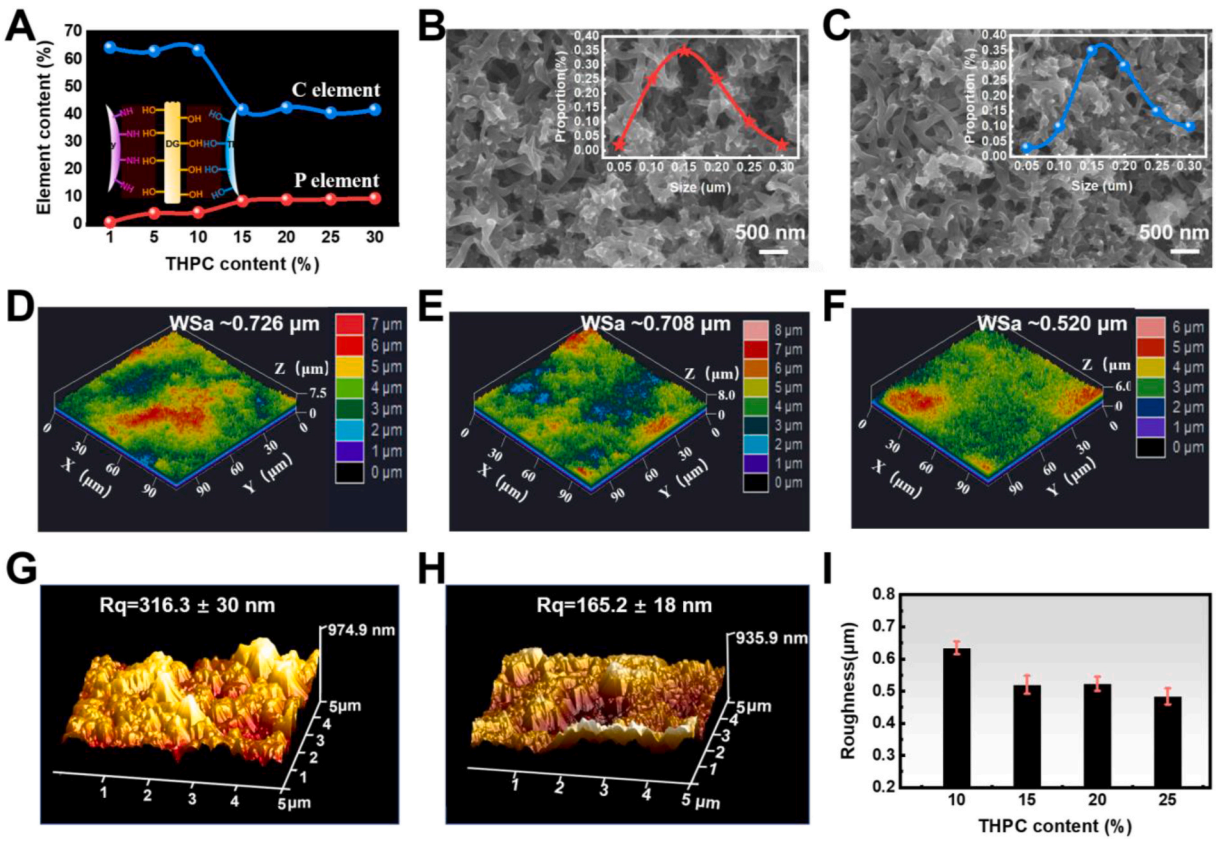

Fig. 4. (A) Element content change of the PPy@DG/THPC membrane along with the addition of THPC. (B–C) SEM images of the PPy@DG/THPC membrane with 25% THPC and 35% THPC, and their diameter size distribution of PPy@DG/THPC-25 and PPy@DG/THPC-35. CLSM images the (D) PPy membrane, (E) PPy@DG membrane, and (F) PPy@DG/THPC-15 membrane. AFM images of (G) the PPy@DG membrane and (H) PPy@DG/THPC membrane. (I) Roughness of the PPy@DG/THPC composite membrane with the addition of THPC.

~1.5 s and ~2.5 s, respectively (Figure S8). This may be because a small amount of THPC molecules resulted in the large pore size in the Py@DG/THPC-10 membrane. In comparison, excessive THPC molecules may bring a prolonged water molecule transmission path.

The zeta potential under different pH conditions was further surveyed. As displayed in Fig. 5B, the zeta potentials showed a gradual decrease trend from the acidic to the alkaline environments. The zeta potential of the PPy@DG/THPC-15 membrane (−22.95 ± 0.81 eV) was litter than the PPy membrane (−5.31 ± 0.49 eV) and PPy@DG membrane (−18.7 ± 0.76 eV) under pH = 7. This result was due to the differential element contents in these membranes (Fig. 3I). Besides, the sunlight absorption capacity of these membranes was studied. The nylon substance showed a low sunlight absorption capacity. The light absorption ability of the PPy@DG membrane increased to ~82.4% of total solar energy in the wavelengths from 550 to 2500 nm (Fig. 5C). However, the sunlight absorption ability of the PPy@DG/THPC-15 membrane reached up to ~97.6% because of its coral-like hierarchical nanostructure, indicating the excellent sunlight absorption performance of this membrane.

Furthermore, the light-to-heat conversion capability was evaluated. The maximal surface temperature of the PPy@DG/THPC-15 membrane increased from 33.2 °C to 43.3 °C within 5 min, which was higher than the PPy@DG membrane (Figure S9A). And there was a litter change in the PPy@DG/THPC membrane with varying contents of THPC. The surface temperature of the PPy@DG/THPC-15 membrane with varying dispersion volumes was studied. The dispersion volume has a distinct effect on the light-to-heat conversion performance. The low dose dispersion brought about lower surface temperature, resulting from the reflection effect of the substrate. The excessive dispersion resulted in the shedding phenomenon of the substance (Figure S9B). Besides, the PPy@DG/THPC-15 membrane presented a good light-to-heat conversion ability under different sun illuminations (Figure S9C).

The PPy@DG/THPC-15 membrane with excellent light absorption capacity was applied for water purification. The evaporation rate of this membrane for pure water was up to 1.47 ± 0.05 kg/m^2/h under 1-sun illumination (Fig. 5D). For one thing, the hydrophilic functional group can facilitate the water absorption process through capillary and H-bond effects (Fig. 5E) [56]. For another, excessive H-bond was not conducive to escaping water vapour from the membrane during evaporation [36]. This membrane was also served as a photothermal layer for the saline water distillation. The polymer network channels offered sufficient water for evaporation. Therefore, it showed excellent evaporation ability for 3.5 wt% saline water with a maximum rate of 1.46 ± 0.02 kg/m^2/h under 1-sun illumination (Fig. 5F). Moreover, the evaporation capacity of the PPy@DG/THPC-15 membrane was achieved best when the volume dosage of the PPy dispersion was 3 mL (Fig. 5G). This was because cracks occurred on the membrane surface with the dispersion dosage (4 mL).

In addition, it displayed superior evaporation performance for saline water with different concentrations. The evaporation rate of this membrane was close to 1.27 ± 0.05 kg/m^2/h, 1.18 ± 0.04 kg/m^2/h, 1.12 ± 0.07 kg/m^2/h, 1.08 ± 0.05 kg/m^2/h, 0.82 ± 0.02 kg/m^2/h when the concentration of NaCl solution was 5%, 10%, 15%, 20%, and 36% (saturated state), respectively (Fig. 5H). Moreover, the PPy@DG/THPC-15 membrane almost kept its performance after the cyclic evaporation process when the concentrations of NaCl solution were 10% and 20% (Figure S10). Furthermore, the conductivity reduced from ~75.2 ms to ~13.96 μs, from ~122.4 ms to ~49.71 μs, respectively, indicating the effective evaporation capacity of the PPy@DG/THPC-15 membrane. Besides, the evaporation ability of the PPy@DG/THPC-15 membrane

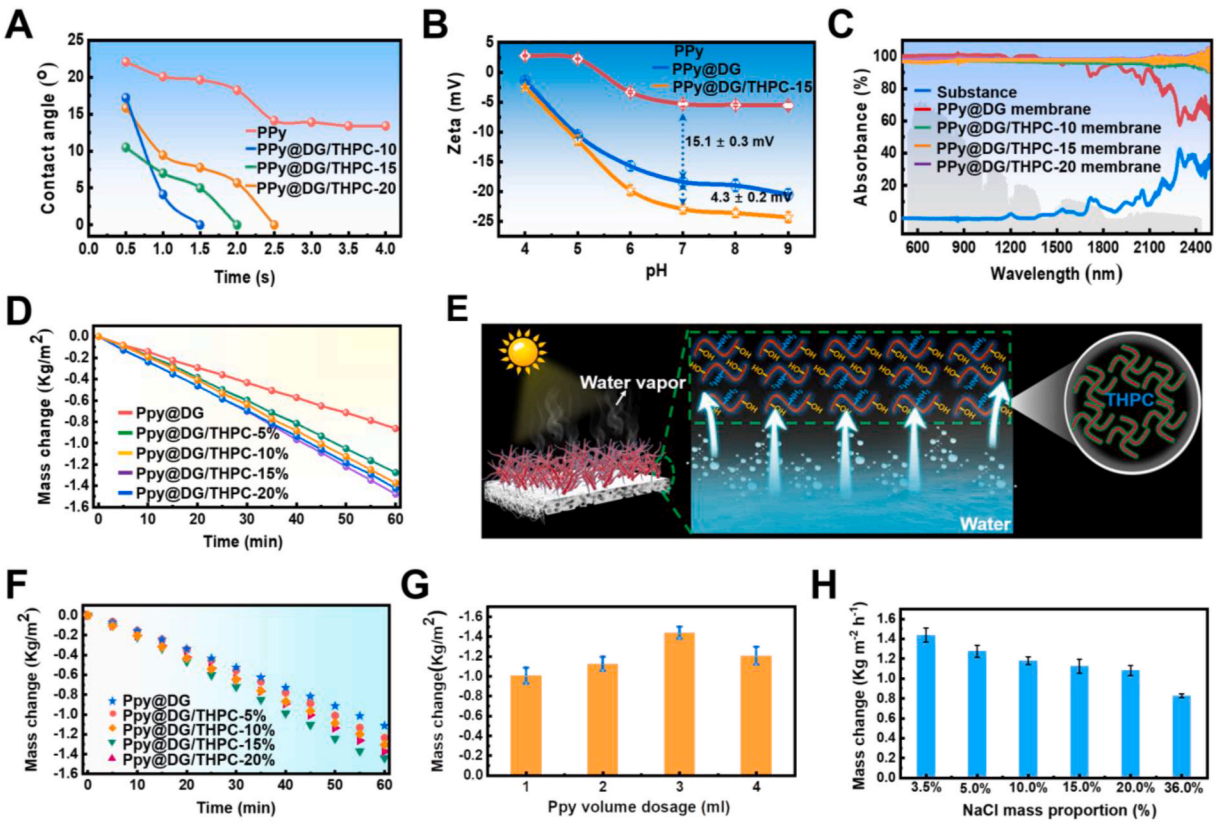

Fig. 5. (A) Contact changes of the PPy@DG/THPC membrane with different THPC contents. (B) Zeta potentials of the PPy membrane, PPy@DG membrane, and PPy@DG/THPC-15 membrane under different pH conditions. (C) UV/Vis spectrum of the substance, PPy@DG membrane, and PPy@DG/THPC membrane with different THPC contents. (D) Water mass changes over time of different membranes. (E) Schematic diagram of the water evaporation process of the PPy@DG/THPC-15 membrane. (F) Evaporation rates of different membranes for 3.5 wt% saline water. (G) Evaporation rates of the PPy@DG/THPC-15 membrane with varying dispersion volumes for 3.5 wt% saline water. (H) Evaporation rates of the PPy@DG/THPC-15 membrane for saline water with varying concentrations. (Noting: evaporation process was irradiated under 1-sun unless otherwise specified).

gradually enhanced along with the increase of solar intensity (Figure S11A). The salt-resistant performance of this membrane was also investigated. When the PPy@DG/THPC-15 membrane was floating on the water, 1.0 g/cm NaCl solid was added to its surface. The NaCl disappeared and dissolved into the water after 8 h under 1-sun irradiation (Figure S11B). Furthermore, periodical solar desalination was performed to assess its steady salt rejection ability. This membrane was alternately floated on the saline water (3.5 wt%) under illumination for 1 h and placed in the dark environment for 30 min. The results indicated litter solar evaporation capacity decreased after 20 cycles with 1.46 ± 0.02 kg/m^2/h (Fig. 6A). The evaporation efficiency (η) of the PPy@DG/THPC-15 membrane for saline water (3.5 wt%) was calculated. The surrounding temperature was 33.4 °C. The evaporation efficiency of this membrane was ~83.9% under a power density of 1 kW/m^2. Meanwhile, after desalination, the concentrations of various ions, including, Na^+, K^+, Ca^{2+}, Mg^{2+}, were significantly reduced by more than 98.2% (Fig. 6B), which was far below the standards of the World Health Organization [33]. The excellent salt-rejecting performance was under the joint of capillary channels and charges effect. On the one hand, the capillary channels offered sufficient water toward the evaporation membrane surface and subsequently transported the enriched salt ions into the bulk water under a concentration gradient [57]. On the other hand, PPy@DG/THPC-15 membrane presented abundant negative charges. The salts were trapped in the polymer network to avoid salt contamination (Fig. 6C) [45].

In addition, the PPy@DG/THPC-15 membrane showed good evaporation ability for water containing heavy metals (Figure S12). The copper chloride ($CuCl_2$) and Ferric chloride ($FeCl_3$) solutions became clear, and their conductivity reduced from 18.16 ± 1.21 ms to 2.32 ± 0.92 μs, from 32.13 ± 1.92 ms to 2.04 ± 0.56 μs, respectively, indicating the effective water purification of this membrane. The PPy@DG/THPC-15 membrane can also be applied for the solar evaporation of oil-in-water (O/W) emulsion. As shown in Fig. 6D, the evaporation rate of the heptane-in-water (H/W) emulsion, chloroform-in-water (C/W) emulsion, and dichloromethane-in-water (D/W) emulsion was attained to 1.21 ± 0.02 kg/m^2/h, 1.32 ± 0.03 kg/m^2/h, and 1.41 ± 0.05 kg/m^2/h, respectively. Moreover, the PPy@DG/THPC-15 membrane showed stable evaporation performance for C/W emulsion with a rate of 1.32 ± 0.02 kg/m^2/h even after the long-term evaporation (Fig. 6D). The evaporation condensate water became transparent with the efficiency of 99.17 ± 0.42%, 99.65 ± 0.37%, 99.32 ± 0.29%, respectively. (Figure S13-**S14**).

Experiments were also carried out to survey the evaporation ability of the PPy@DG/THPC-15 membrane for various dye solutions (20 mg/L). As presented in Figure S15, the evaporation rate of methyl orange (MO), methylene azure II (MAII), methyl blue (^{MB}), evans blue (EB), rose bengal-94 (RB-94) solutions can reach 1.47 ± 0.06 kg/m^2/h, 1.45 ± 0.04 kg/m^2/h, 1.46 ± 0.01 kg/m^2/h, 1.47 ± 0.06 kg/m^2/h, 1.48 ± 0.05 kg/m^2/h, respectively, indicating its evaporation rate has not been affected regardless of the molecular weights, charges of the dye molecules (Table S1). In addition, the evaporation efficiency of these dye solutions was all up to ~96.78% (Fig. 6E, S16), further indicating its excellent anti-fouling ability during the evaporation process. On the one hand, the hydration layer of this membrane can restrain the oil droplets from the membrane surface [58–60]. On the other hand, abundant negative charges can effectively reject various pollutants [45]. Therefore, it kept its superior evaporation ability and micromorphology with rates of 1.36 ± 0.04 kg/m^2/h, 1.37 ± 0.03 kg/m^2/h,1.45 ± 0.06

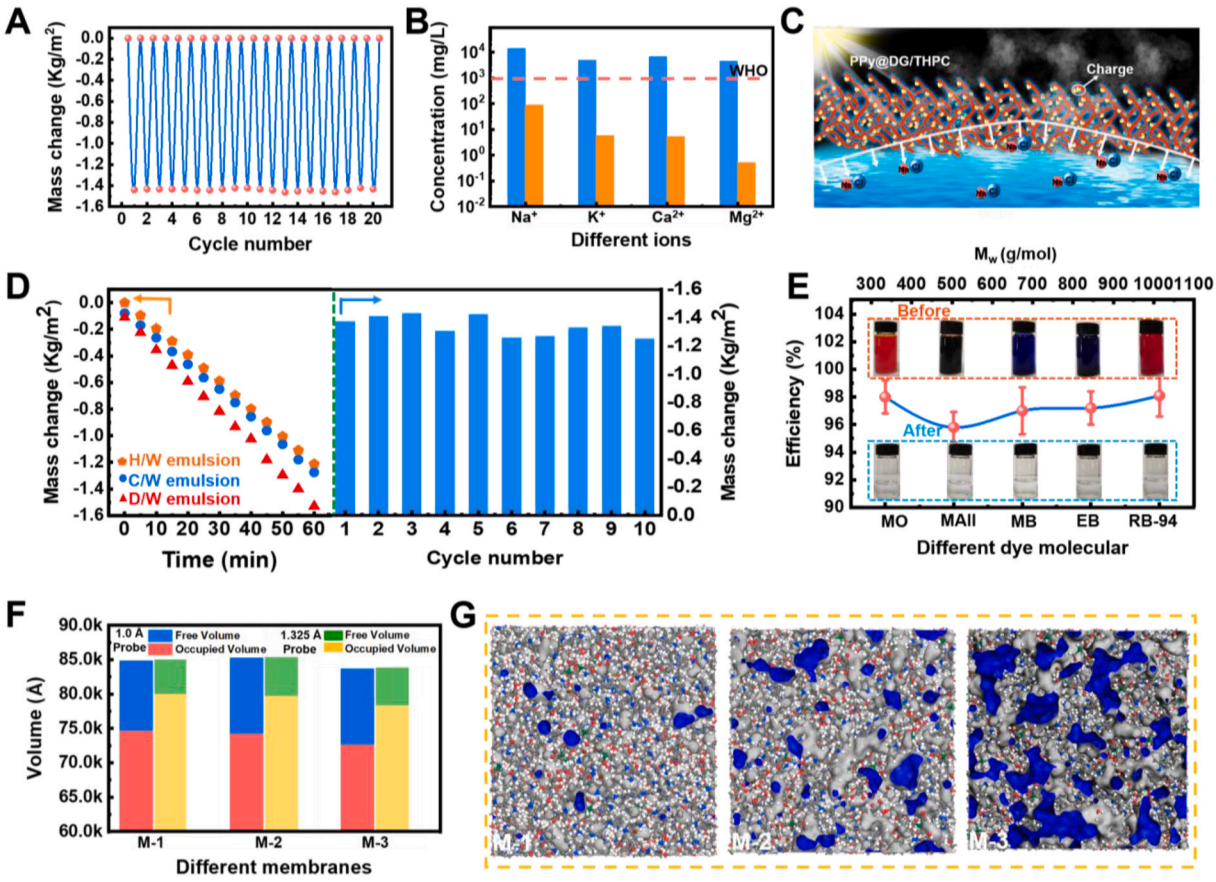

Fig. 6. (A) Cyclical evaporation of the PPy@DG/THPC-15 membrane for 3.5 wt% saline water under 1-sun illumination. (B) Schematic diagram of PPy@DG/THPC-15 membrane for the resistance of the accumulation and enrichment of salt ions. (C) Primary ions in a simulated seawater sample before and after desalination. (D) Mass change of the PPy@DG/THPC-15 membrane for different O/W emulsions (left) and its cyclical evaporation ability for C/W emulsion (right) under 1-sun illumination. (E) Evaporation efficiency and their responding photographs of the PPy@DG/THPC-15 membrane for dye molecules. (F) Free volume and total space volume of different membranes under different probes (M-1: PPy@DG/THPC-5; M-2: PPy@DG/THPC-10; M-3: PPy@DG/THPC-15). (G) Molecular simulation of the free volume of different membranes from the plane perspective, PPy@DG/THPC-5, PPy@DG/THPC-10, PPy@DG/THPC-15 (from left to right). The blue part was the FFV.

kg/m^2/h, 1.46 ± 0.04 kg/m^2/h, under harsh conditions including, sodium hydroxide (NaOH), hydrochloric acid (HCl), humic acid (HA) and bovine serum albumin (BSA) (Figure S17-**18**). In addition, the PPy@DG/THPC-15 membrane almost maintained its photothermal evaporation capacity after being bent, indicating its good mechanical stability (Figure S19).

Molecular dynamics simulations characterized different membranes' fractional free volumes (FFV). The simulation models were constructed in the Amorphous Cell module in Materials Studio. The cells were equilibrated by energy minimization and performed several MD simulations in an ensemble for more than 10 ns The initial packing densities were 1.0 g/cm^3 and then gradually compressed to the target densities. The atom volumes and surfaces module in Materials Studio was used to evaluate the FFV, and the Connolly radius was selected as 1.000 Å and 1.325 Å. As shown in Fig. 6F, the PPy@DG/THPC-15 membrane's FFV ratios were ~14.20% and ~6.86% under the Connolly radius of 1.000 Å and 1.325 Å, respectively, which were higher than the PPy@DG/THPC-5 membrane and PPy@DG/THPC-10 membrane (Fig. 6F–G, S20). Moreover, the FFV of the PPy@DG/THPC-15 membrane was higher than that of the PPy@DG/THPC-20 membrane (Figure S21). This may be due to the block of part of the pore structure due to excessive THPC modification. Hence, the evaporation performance of the PPy@DG/THPC-15 membrane was slightly higher than the PPy@DG/THPC-20 membrane (~1.42 kg/m^2/h) (Fig. 5F). In addition, for comparison, the1-APi and [EtPy][Br] were also applied to modify the PPy@DG membrane, respectively. Several tests were carried out to verify the functionalization of the1-APi and [EtPy][Br] on the PPy@DG membrane (Figure S22-S25). The evaporation rates of the PPy@DG/1-APi and PPy@DG/[EtPy][Br] composite membranes were ~1.32 kg/m^2/h and ~1.25 kg/m^2/h, respectively, which was lower than the PPy@DG/THPC-15 composite membrane (Figure S26A). Besides, the FFV of the PPy@DG/THPC-15 membrane was higher than the PPy@DG/1-APi and PPy@DG/[EtPy][Br] membranes (Figure S26B-26C). The high free volume of the PPy@DG/THPC-15 membrane was conducive to inhibiting the salts accumulation [48–50]. In addition, abundant negative charges endowed the PPy@DG/THPC-15 membrane with excellent salt-resistance and anti-fouling abilities (Fig. 5B). Hence, under the synergy of the hierarchical nanostructure, abundant charges, and high free volume, the PPy@DG/THPC-15 membrane presented superior evaporation performance.

4. Conclusions

In conclusion, a coral-like PPy-based membrane was presented through the interfacial modification of DG and THPC. The PPy@DG/THPC membrane exhibited a broad sunlight absorption capacity with an efficiency of ~97.6% because of its hierarchical nanostructure. Moreover, due to the introduction of THPC, this membrane showed good hydrophilic ability and rich charges, giving it excellent salt-resistance property. Furthermore, molecular dynamics simulations indicated the high free volume of the PPy@DG/THPC membrane for inhibiting salt crystallization. Therefore, this membrane presented an excellent

evaporation performance with 1.46 ± 0.02 kg/m^2/h in simulated brine (3.5 wt% NaCl) under 1-sun illumination. In addition, the PPy@DG/THPC-15 membrane exhibited exceptional anti-fouling ability under the collaboration of hydration and charge effect. Hence, the PPy@DG/THPC-15 membrane can achieve sustainable solar evaporation to produce freshwater, intercept complex organic contaminants, and obtain water to meet drinking-water standards. These features make the PPy@DG/THPC membrane a good choice for salt-free solar-enabled water purification.

Credit author statement

Jincui Gu: Conceptualization, Investigation, Resources, Data curation, Writing – original draft; Peng Xiao: Conceptualization, Validation, Writing – review & editing; **Jianmin Guan**: Visualization, Supervision, Formal analysis; **Feng Ni**: Conceptualization, Supervision, Methodology; **Chang Zhang**: Formal analysis, Supervision, Resources; **Weiqing Yang:** Data curation, Supervision; **Qingquan Liu**: Visualization, Supervision; **Tao Chen**: Conceptualization, Resources, Project administration, Writing – review & editing.

Author contributions

Jincui Gu and **Peng Xiao** proposed experimental ideas and designed experimental ideas. **Jincui Gu**, **Jianmin Guan**, and **Feng Ni** carried out experimental exploration and performed a series of characterizations. **Chang Zhang, Weiqing Yang**, and **Qingquan Liu** supervised the experiment process and verified the results. **Jincui Gu** and **Peng Xiao** organized data and wrote manuscripts. Tao Chen supervised the project and edited the manuscript.

Declaration of competing interest

The authors declare that they have no known competing financial interests or personal relationships that could have appeared to influence the work reported in this paper.

Acknowledgements

Thanks for the help from Lingtong Ji Wuhan University. We are grateful for financial support from the Ningbo Public Welfare Science and Technology Plan Project (2021S150), Ningbo Science and Technology Bureau (2021Z127), Open Research Fund of Key Laboratory of Marine Materials and Related Technologies (2013DP173296, 2019K03), K. C. Wong Education Foundation (GJTD-2019-13).

Appendix A. Supplementary data

Supplementary data to this article can be found online at https://doi.org/10.1016/j.mtphys.2022.100715.

References

[1] X. Zhou, Y. Guo, F. Zhao, W. Shi, G. Yu, Topology-controlled hydration of polymer network in hydrogels for solar-driven wastewater treatment, Adv. Mater. 32 (2020) 2007012–2007018, https://doi.org/10.1002/adma.202007012.

[2] Y.M. Zhang, X.S. Chen, C.J. Luo, J.C. Gu, M.R. Li, M. Chao, X. Chen, T. Chen, L. K. Yan, X. Wang, Column-to-Beam structure house inspired MXene-based integrated membrane with stable interlayer spacing for water purification, Adv. Funct. Mater. (2022) 2111660, https://doi.org/10.1002/adfm.202111660.

[3] X.Q. Fan, Y. Yang, X.L. Shi, Y. Liu, H.P. Li, J.J. Liang, Y.S. Chen, A MXene-based hierarchical design enabling highly efficient and stable solar-water desalination with good salt-resistance, Adv. Funct. Mater. 30 (2020) 2007110–2007120, https://doi.org/10.1002/adfm.202007110.

[4] F.B. Zhu, L.Q. Wang, B. Demir, M. An, Z.L. Wu, J. Yin, R. Xiao, Q. Zheng, J. Qian, Accelerating solar desalination in brine through ion activated hierarchically porous polyion complex hydrogels, Mater. Horiz. 7 (2020) 3178–3195, https://doi.org/10.1039/D0MH01259A.

[5] Y.D. Wang, X. Wu, P. Wu, Ji Y. Zhao, X.F. Yang, G. Owens, H.L. Xu, Enhancing solar steam generation using a highly thermally conductive evaporator support, Sci. Bull. 66 (2021) 2479–2488, https://doi.org/10.1016/j.scib.2021.09.018.

[6] H.J. Zheng, X. Li, K.J. Zhu, P.H. Liang, M. Wu, Y. Rao, R. Jian, F. Shi, J. Wang, K. Yan, J.S. Liu, Colloidal carbon quantum dots as light absorber for efficient and stable ecofriendly photoelectrochemical hydrogen generation, Nano Energy 93 (2022) 106831. https://10.1016/j.nanoen.2021.106122.

[7] C.L. Zhang, Y. Shi, L. Shi, H.X. Li, R.Y. Li, S. Hong, S.F. Zhuo, T. Zhang, P. Wang, Designing a next generation solar crystallizer for real seawater brine treatment with zero liquid discharge, Nat. Commun. 12 (2021) 998–1007, https://doi.org/10.1038/s41467-021-21124-4.

[8] Z.Y. Sun, J.J. Wang, Q.L. Wu, Z.Y. Wang, Z. Wang, J. Sun, C.J. Liu, Plasmon based double-layer hydrogel device for a highly efficient solar vapor generation, Adv. Funct. Mater. 29 (2019) 1901312–1901318, https://doi.org/10.1002/adfm.201901312.

[9] M.M. Zou, Y. Zhang, Z.R. Cai, C.X. Li, Z.Y. Sun, C.L. Yu, Z.C. Dong, L. Wu, Y. L. Song, 3D printing a biomimetic bridge-arch solar evaporator for eliminating salt accumulation with desalination and agricultural applications, Adv. Mater. 34 (2021) 2102443–2102454, https://doi.org/10.1002/adma.202102443.

[10] W.X. Guan, Y.H. Guo, G.H. Yu, Carbon materials for solar water evaporation and desalination, Small 17 (2021) 2007176–2007192, https://doi.org/10.1002/smLl.202007176.

[11] Y. Lu, D.Q. Fan, Z.Y. Shen, H. Zhang, H.L. Xu, X.F. Yang, Design and performance boost of a MOF-functionalized-wood solar evaporator through tuning the hydrogen-bonding interactions, Nano Energy 95 (2022) 107016, https://doi.org/10.1016/j.nanoen.2022.107016.

[12] Q. Zhang, G. Yi, Z. Fu, H.T. Yu, S. Chen, X. Quan, Vertically aligned Janus MXene-based aerogels for solar desalination with high efficiency and salt-resistance, ACS Nano 13 (2019) 13196–13207, https://doi.org/10.1021/acsnano.9b06180.

[13] C.J. Chen, Y.D. Kuang, L.B. Hu, Challenges and opportunities for solar evaporation, Joule 3 (2019) 683–718, https://doi.org/10.1016/j.joule.2018.12.023.

[14] Z.X. Wang, M.C. Han, F. He, S.Q. Peng, S. Darling, Y.X. Li, Versatile coating with multifunctional performance for solar steam generation, Nano Energy 74 (2020) 104886–104896, https://doi.org/10.1016/j.nanoen.2020.104886.

[15] Y. Xu, J.J. Ma, D.Q. Liu, H.B. Xu, F.Y. Cui, W. Wang, Origami system for efficient solar driven distillation in emergency water supply, Chem. Eng. J. 356 (2019) 869–876, https://doi.org/10.1016/j.cej.2018.09.070.

[16] Z.M. Huang, S.L. Li, X. Cui, Y.P. Wan, Y.F. Xiao, S. Tian, H. Wang, X.Z. Li, Q. Zhao, C.S. Lee, A broadband aggregation-independent plasmonic absorber for highly efficient solar steam generation, J. Mater. Chem. 8 (2020) 10742–10746, https://doi.org/10.1039/D0TA01980A.

[17] X.H. Liu, D. Mishr, X.B. Wang, H.Y. Peng, C.Q. Hu, Towards highly efficient solar-driven interfacial evaporation for desalination, J. Mater. Chem. 8 (2020) 17907–17937, https://doi.org/10.1039/C9TA12612K.

[18] S.W. Sharshir, A.M. Algazzarc, K.A. Elmaadawy, A.W. Kandeal, M.R. Elkadeem, T. Arunkumar, J.F. Zang, N. Yang, New hydrogel materials for improving solar water evaporation, desalination and wastewater treatment: a review, Desalination 491 (2020) 114564–114581, https://doi.org/10.1016/j.desal.2020.114564.

[19] Y.Y. Li, N. Chen, Z.L. Li, H.B. Shao, X.T. Sun, F. Liu, X.T. Liu, Q. Guo, L.T. Qu, Reborn three-dimensional graphene with ultrahigh volumetric desalination capacity, Adv. Mater. 33 (2021) 2105853–2105863, https://doi.org/10.1002/adma.202105853.

[20] Q. Hou, C.R. Xue, N. Li, H.Q. Wang, Q. Chang, H.T. Liu, J. Yang, S.L. Hu, Self-assembly carbon dots for powerful solar water evaporation, Carbon 149 (2019) 556–563, https://doi.org/10.1016/j.carbon.2019.04.083.

[21] D.P. Qi, Y. Liu, Y.B. Liu, Z.Y. Liu, Y.F. Luo, H.B. Xu, X. Zhou, J.J. Zhang, H. Yang, W. Wang, X.D. Chen, Polymeric membranes with selective solution-diffusion for intercepting volatile organic compounds during solar-driven water remediation, Adv. Mater. 32 (2020) 2004401–2004409, https://doi.org/10.1002/adma.202004401.

[22] Z. Wang, Y.T. Yan, X.P. Shen, C.D. Jin, Q.F. Sun, H.Q. Li, A wood-polypyrrole composite as a photothermal conversion device for solar evaporation enhancement, J. Mater. Chem. 7 (2019) 20706–20712, https://doi.org/10.1039/C9TA04914B.

[23] P. Wu, X. Wu, H.L. Xu, G. Owens, Interfacial solar evaporation driven lead removal from a contaminated soil, EcoMat 3 (2021): e12140, https://doi.org/10.1002/eom2.12140.

[24] L.L. Zhu, T.P. Ding, M.M. Gao, C.K.N. Peh, G.W. Ho, Shape conformal and thermal insulative organic solar absorber sponge for photothermal water evaporation and thermoelectric power generation, Adv. Energy Mater. 9 (2019) 1900250–1900256, https://doi.org/10.1002/aenm.201900250.

[25] G.G. Chen, T. Li, C.J. Chen, W.Q. Kong, M.L. Jiao, B. Jiang, Q.Q. Xia, Z.Q. Liang, Y. Liu, S.M. He, L.B. Hu, Scalable wood hydrogel membrane with nanoscale channels, ACS Nano 15 (2021) 11244–11252, https://doi.org/10.1021/acsnano.0c10117.

[26] Z.X. Wang, X.C. Wu, F. He, S.Q. Peng, Y.X. Li, Confinement capillarity of thin coating for boosting solar-driven water evaporation, Adv. Funct. Mater. 31 (2021) 2011114–2011121, https://doi.org/10.1002/adfm.202011114.

[27] H.Q. Wang, C. Zhang, Z.H. Zhang, B. Zhou, J. Shen, A. Du, Biomimetic ultra-black sponge derived from loofah and Co-MOF for long-term solar-powered vapor generation and desalination, Sol. RRL 5 (2021) 2000817–2000825, https://doi.org/10.1002/solr.202000817.

[28] Q.L. Ma, P.F. Yin, M.T. Zhao, Z.Y. Luo, Y. Huang, Q.Y. He, Y.F. Yu, Z.Q. Liu, Z. N. Hu, B. Chen, H. Zhang, MOF-based hierarchical structures for solar-thermal clean water production, Adv. Mater. 31 (2019) 1808249–1808255, https://doi.org/10.1002/adma.201808249.

[29] Z.W. Lei, X.T. Sun, S.F. Zhu, K. Dong, X.Q. Liu, L.L. Wang, X.S. Zhang, L.J. Qu, X. J. Zhang, Nature inspired MXene-decorated 3D honeycomb-fabric architectures toward efficient water desalination and salt harvesting, Nano-Micro Lett. 14 (2022) 10, https://doi.org/10.1007/s40820-021-00748-7.
[30] L.J. Zhu, M.M. Gao, C.K.N. Peh, G. Wei, Recent progress in solar-driven interfacial water evaporation: advanced designs and applications, Nano Energy 57 (2019) 507–518, https://doi.org/10.1016/j.nanoen.2018.12.046.
[31] Q.C. Lu, W.X. Shi, H.Z. Yang, X. Wang, Nanoconfined water-molecule channels for high-yield solar vapor generation under weaker sunlight, Adv. Mater. 32 (2020) 2001544–2001550, https://doi.org/10.1002/adma.202001544.
[32] S. Qin, D. Liu, Y. Chen, C. Chen, G. Wang, Wang, J.M. Razal, W.W. Lei, Nanofluidic electric generators constructed from boron nitride nanosheet membranes, Nano Energy 47 (2018) 368–373, https://doi.org/10.1016/j.nanoen.2018.03.030.
[33] G.L. Yang, W.W. Lei, C. Chen, S. Qin, L.Z. Zhang, Y.Y. Su, J.M. Wang, Z.Q. Chen, L. Sun, X.G. Wang, D. Liu, Ultrathin $Ti_3C_2T_x$ (MXene) membrane for pressure-driven electrokinetic power generation, Nano Energy 75 (2020) 104954–104976, https://doi.org/10.1016/j.nanoen.2020.104954.
[34] K.Y. Xu, C.B. Wang, Z.T. Li, S.M. Wu, J.L. Wang, Salt mitigation strategies of solar-driven interfacial desalination, Adv. Funct. Mater. 31 (2020) 2007855–2007880, https://doi.org/10.1002/adfm.202007855.
[35] F.T. Meng, B.Z. Ju, S.F. Zhang, B.T. Tang, Nano/microstructured materials for solar-driven interfacial evaporators towards water purification, J. Mater. Chem. 9 (2021) 13746–13769, https://doi.org/10.1039/D1TA02202D.
[36] Z.X. Liu, Z. Zhou, N.Y. Wu, R.Q. Zhang, B. Zhu, H. Jin, Y.M. Zhang, M.F. Zhu, Z. G. Chen, Hierarchical photothermal fabrics with low evaporation enthalpy as heliotropic evaporators for efficient, continuous, salt-free desalination, ACS Nano 15 (2021) 13007–13018, https://doi.org/10.1021/acsnano.1c01900.
[37] Y.W. Yang, H.Y. Zhao, Z.Y. Yin, J.Q. Zhao, X.T. Yin, N. Li, D.D. Yin, Y.N. Li, B. Lei, Y.P. Du, W.X. Que, A general salt-resistant hydrophilic/hydrophobic nanoporous double layer design for efficient and stable solar water evaporation distillation, Mater. Horiz. 5 (2018) 1143–1150, https://doi.org/10.1039/C8MH00386F.
[38] J.X. Chen, J.L. Yin, B. Li, Z.Y. Ye, D.L. Liu, D. Ding, F. Qian, N. Myung, Q. Zhang, Y. D. Yin, Janus evaporators with self-recovering hydrophobicity for salt-rejecting interfacial solar desalination, ACS Nano 14 (2020) 17419–17427, https://doi.org/10.1021/acsnano.0c07677.
[39] W.C. Xu, X.Z. Hu, S.D. Zhuang, Y.X. Wang, X.Q. Li, L. Zhou, S.N. Zhu, J. Zhu, Flexible and salt resistant Janus absorbers by electrospinning for stable and efficient solar desalination, Adv. Energy Mater. 8 (2018) 1702884–1702889, https://doi.org/10.1002/aenm.201 L.702884.
[40] H.Y. Zhao, J. Zhou, Z.L. Yu, L.F. Chen, H.J. Zhan, H.W. Zhu, J. Huang, L.A. Shi, S. H. Yu, Lotus-inspired evaporator with Janus wettability and bimodal pores for solar steam generation, Cell Rep. Phys. Sci. 1 (2020) 100074–100090, https://doi.org/10.1016/j.xcrp.2020.100074.
[41] S.W. Yan, H.J. Song, Y. Li, J. Yang, X.H. Jia, S.Z. Wang, X.F. Yang, Integrated reduced graphene oxide/polypyrrole hybrid aerogels for simultaneous photocatalytic decontamination and water evaporation, Appl. Catal., B 301 (2022) 120820, https://doi.org/10.1016/j.apcatb.2021.120820.
[42] X. Wu, Y.D. Wang, P. Wu, J.Y. Zhao, Y. Lu, X.F. Yang, H.L. Xu, Dual-zone photothermal evaporator for antisalt accumulation and highly efficient solar steam generation, Adv. Funct. Mater. 31 (2021) 2102618, https://doi.org/10.1002/adfm.202102618.
[43] Y. Shi, O. Ilic, H.A. Atwater, J.R. Greer, All-day fresh water harvesting by microstructured hydrogel membranes, Nat. Commun. 12 (2021) 2797–2806, https://doi.org/10.1038/s41467-021-23174-0.
[44] W. Cao, L.L. Huang, M. Ma, L.H. Lu, X.H. Lu, Water in narrow carbon nanotubes: roughness promoted diffusion transition, J. Phys. Chem. C 122 (2018) 19124–19132, https://doi.org/10.1021/acs.jpcc.8b02929.
[45] Q.B. Xiao, Y. Zhu, Y.L. Xi, X.P. Kong, X.M. Ye, Z.Y. Zhang, C.P. Qiu, W.L. Xu, S. Cheng, J. Zhang, M.L. Jia, E.H. Sun, H.Z. Lin, J. Wang, Highly charged hydrogel with enhanced donnan exclusion toward ammonium for efficient solar-driven water remediation, Chem. Eng. J. 430 (2022) 133019, https://doi.org/10.1016/j.cej.2021.133019.
[46] W. Zhang, Z.H. Pan, F.K. Yang, B.X. Zhao, A facile in situ approach to polypyrrole functionalization through bioinspired catechols, Adv. Funct. Mater. 25 (2015) 1588, https://doi.org/10.1002/adfm.201403115.
[47] H.W. Peng, W.H. Zhang, W.S. Hung, N.X. Wang, J. Sun, K.R. Lee, Q.F. An, C.M. Liu, Q. Zhao, Phosphonium modification leads to ultrapermeable antibacterial polyamide composite membranes with unreduced thickness, Adv. Mater. 32 (2020) 2001383–2001389, https://doi.org/10.1002/adma.202001383.
[48] Z. Ali, B. Ghanem, Y.G. Wang, F. Pacheco, W. Ogieglo, H. Vovusha, G. Genduso, U. Schwingenschlögl, Y. Han, I. Pinnau, Finely tuned submicroporous thin-film molecular sieve membranes for highly efficient fluid separations, Adv. Mater. 32 (2020) 2001132–2001138, https://doi.org/10.1002/adma.202001132.
[49] N. Petzetakis, C.M. Doherty, A.W. Thornton, X.C. Chen, P. Cotanda, A. Hill, N. Balsara, Membranes with artificial free-volume for biofuel production, Nat. Commun. 6 (2015) 7529–7536, https://doi.org/10.1038/ncomms8529.
[50] T.E. Culp, B. Khara, K.P. Brickey, M. Geitner, T.J. Zimudzi, J.D. Wilbur, S.D. Jons, A. Roy, M. Paul, B. Ganapathysubramanian, A.L. Zydney, M. Kumar, E.D. Gomez, Nanoscale control of internal inhomogeneityenhances water transport in desalination membranes, Science 371 (2021) 72–75, https://doi.org/10.1126/science.abb8518.
[51] F. Ni, P. Xiao, N.X. Qiu, C. Zhang, Y. Liang, J.C. Gu, J.Y. Xia, Z.X. Zeng, L.P. Wang, Q.J. Xue, T. Chen, Collective behaviors mediated multifunctional black sand aggregate towards environmentally adaptive solar-to-thermal purified water harvesting, Nano Energy 68 (2020) 104311–104343, https://doi.org/10.1016/j.nanoen.2019.104311.
[52] N. Guimarda, N. Gomez, C. Schmidt, Conducting polymers in biomedical engineering, Prog. Polym. Sci. 32 (2007) 876–921, https://doi.org/10.1016/j.progpolymsci.2007.05.012.
[53] A. Vaish, S. Roy, P. De, Synthesis of amino acid based covalently cross-linked polymeric gels using tetrakis (hydroxymethyl) phosphonium chloride as a cross-linker, Polymer 58 (2015) 1–8, https://doi.org/10.1016/j.polymer.2014.12.043.
[54] J.C. Gu, T.Y. Chen, P. Xiao, F. Ni, L.K. Yan, Y.J. Nie, T. Chen, Constructing oxidized carbon spheres-based heterogeneous membrane with high surface energy for energy-free water purification, Chem. Eng. J. 431 (2022) 134132, https://doi.org/10.1016/j.cej.2021.134132.
[55] M. Imani, A. Ghasemian, M. Firouzabadi, E. Afra, M. Borghei, L. Johansson, P. Gane, O.J. Rojas, Coupling nanofibril lateral size and residual lignin to tailor the properties of lignocellulose films, Adv. Mater. Interfac. 6 (2019) 1900770–1900778, https://doi.org/10.1002/admi.201900770.
[56] J.Y. Xia, J.C. Gu, P. Xiao, C. Zhang, L.K. Yan, T. Chen, Supramolecular fabrication of hyperbranched polyethyleneimine toward nanofiltration membrane for efficient wastewater purification, SusMat 1 (2021) 558–568, https://doi.org/10.1002/sus2.33.
[57] S.N. Zhang, J.Y. Huang, Z. Chen, Y.K. Lai, Bioinspired special wettability surfaces: from fundamental research to water harvesting applications, Small 13 (2017) 1602992–1603013, https://doi.org/10.1002/smLl.201602992.
[58] T.Y. Chen, J.Y. Xia, J.C. Gu, G.M. Lu, Q.J. Xue, H.C. Liu, L.K. Yan, T. Chen, Engineering Janus CNTs/OCS composite membrane at air/water interface for excellent dye molecules screening, Chem. Eng. J. 417 (2021) 127947–127956, https://doi.org/10.1016/j.cej.2020.127947.
[59] H. Zhang, Q.M. He, J.Q. Luo, Y.H. Wan, S. Darling, Sharpening nanofiltration: strategies for enhanced membrane selectivity, ACS Appl. Mater. Interfaces 12 (2020) 39948–39966, https://doi.org/10.1021/acsami.0c11136.
[60] X.B. Chen, N.L. Yang, Y.L. Wang, H.Y. He, J.Y. Wang, J.W. Wan, H.Y. Jiang, B. Xu, L.M. Wang, R.B. Yu, L.M. Tong, L. Gu, Q.H. Xiong, C.Y. Chen, S.J. Zhang, D. Wang, Highly efficient photothermal conversion and water transport during solar evaporation enabled by amorphous hollow multishelled nanocomposites, Adv. Mater. 34 (2021) 2107400, https://doi.org/10.1002/adma.202107400.